**RESEARCH**

# Experimental and numerical study of novel Coanda-based unmanned aerial vehicle

Zaid Siddiqi and Jin W. Lee[*]

*Correspondence:
jwlee@ualr.edu

Donaghey College of Science,
Technology, Engineering,
and Mathematics, University
of Arkansas at Little Rock, Little
Rock, AR 72204, USA

## Abstract

Conventional Coanda-based unmanned aerial vehicles (UAV) experience thrust losses in the radial direction. To address these losses, a rectangular, linear arrangement of the Coanda surface was adopted in the proposed novel design. This arrangement minimizes the area change in the radial direction to recover such thrust losses. A prototype of the proposed UAV structure was 3D printed and assembled with a single 9-inch propeller. Performance characteristics of the UAV were evaluated through static testing on a dynamometer under different loading conditions. Experimental results were validated through computational fluid dynamics (CFD) simulations, using the $k$-$\varepsilon$ realizable turbulence model, while the multiple reference frame (MRF) approach was applied in steady state. CFD simulations provided good overall agreement with experimental results having errors less than 8%. Numerical comparison between the novel Coanda design and a conventional Coanda design, having similar radial dimensions, showed that the novel design offered an overall 17% improvement in thrust per the side surface area, thus demonstrating an effective reduction of thrust losses in the radial direction.

**Keywords:** Coanda effect, Unmanned aerial vehicle, Computational fluid dynamics, Multiple reference frame, Thrust, Downwash airspeed

## Introduction

The application of unmanned aerial vehicles (UAVs) has witnessed an unprecedented rise across a wide variety of industries notably the commercial and military sector [1]. Based on specific mission requirements, the objective of most UAV designers is to enhance the aerodynamic performance of their design such that it yields enhanced payload capacity, endurance, and range. An increasingly popular avenue of research in multi-rotor UAVs is harnessing propeller downwash to generate additional lift through the Coanda effect [2]. A lifting force is induced from the Coanda effect when a moving fluid remains attached to a convex surface, thereby creating a low-pressure gradient. UAVs which apply the Coanda effect are generally saucer like in shape and valued particularly for their vertical takeoff and landing (VTOL) capabilities [3]. This design configuration generates lift in two ways: (1) through the rotating propeller(s) located at the center and (2) by radially redirecting propeller downwash over convex Coanda surfaces. In a conference paper published in 2002, Robert Collins [4] presented the application of the Coanda effect

in saucer-shaped UAVs which subsequently led to a patent being granted in 2003 [5]. Geoffrey Hatton [6] in collaboration with GFS Projects introduced a family of Coanda UAVs aptly named GFS (Geoff's Flying Saucers). The GFS UAVs have a circular canopy as a housing for the propulsion system with an orthogonal arrangement of the Coanda surfaces. In 2006, Jean-Louis Naudin [7] made further improvements to the GFS UAVs by introducing an electric engine and made the design, GFS-UAV (N-01A), available to UAV enthusiasts everywhere. In the detailed construction plan, Naudin [7] recommends using propellers ranging from 7 inch in diameter with a pitch of 3 (7 × 3) to 9 inch in diameter with a pitch of 6 inch (9 × 6). To extract higher thrust, many designers applied their own innovative approaches to Coanda-based UAVs such as the addition of helium chambers and tandem rotor arrangement [8].

The proposed novel design, based on a provisional patent [9], establishes the foundation for a thrust generator propulsion system for Coanda-based UAVs [10]. This system aims to replace conventional propellers with an enclosed air compressor to improve propulsive efficiency and overall range by addressing two key design limitations of conventional Coanda UAVs. The first limitation is that these designs commonly suffer from thrust losses experienced by Coanda surfaces due to the radially expanding structure. The presence of these losses is made evident by Ahmed et al. [11] who developed a mathematical model for the flight mechanics of a Coanda UAV and noted that the fluid momentum through a Coanda control volume does not contribute to lift in the tangential (spanwise) direction. The radially expanding design of Coanda UAVs prevents the convex surfaces from behaving similar to a straight wing which generates considerable lift along the linear spanwise direction [12]. The second design limitation is the generation of negative lift by the Coanda UAV's baseplate due to propeller downwash [13]. A keen interest was also taken in Barlow et al. [14]'s study which they began by first experimentally testing the thrust generated by Naudin's UAV [7]. Barlow et al. [14] observed that when compared to a standalone motor propeller, Naudin's UAV [7] generated 34% less thrust due to the negative thrust created by the concave portion of the body. This led Barlow et al. [14] to investigate the application of a propulsion system similar in principle to the Dyson Air Multiplier™ desktop fan. Such a system allowed the incoming airflow to be parallel to the UAV baseplate instead of being perpendicular as was in the case of a propeller. Motivated by Ahmed et al. [11] and Barlow et al. [14]'s observations, the authors conceptualized a novel Coanda UAV design that could address these limitations simultaneously. The objective of this study was focused towards addressing the first design limitation by attempting to minimize the momentum losses that occur due to radial expansion of the fluid as it flows over Coanda surfaces. The proposed solution is that a linear or "straightened" arrangement of Coanda surfaces would be better suited towards restricting fluid momentum losses in the radial direction. Here, the radial direction is considered along the direction of Coanda surfaces' curvature. The details of the first UAV design iteration are further discussed in the "Methods" section. Future iterations of the novel design would address the second limitation by incorporating an enclosed air compressor propulsion system, also called a ring-wing Airfoil, the details of which are further discussed in the "Discussion and future work" section.

The plan to test the proof of concept for the novel Coanda UAV involved two stages: (1) grounded experimental testing of the prototype and (2) validation of the prototype

experimental results at a computational fluid dynamics (CFD) level. The first stage required using a dynamometer (also known as a thrust stand) to measure thrust generated by the system. Dynamometers are widely employed to evaluate motor-propeller performance by using load cells to measure thrust as well as various sensors to measure important performance parameters such as torque and rotational speed. The widespread use of UAVs has led to the commercial availability of dynamometer solutions. Tyto Robotics™ [15] offers a variety of propeller dynamometers based on thrust ratings, specifically the RCbenchmark Series™ thrust stands. To test this two-stage process for evaluating propeller performance cost-effectively on a smaller scale, a precursor study [16] was conducted by the authors to validate experimental propeller results with CFD simulations. In this study [16], experimental trials were performed for a 6-inch propeller using the RCbenchmark™ Series 1580 thrust stand. The CFD simulations provided good overall agreement with the experimental results. Most researchers [17–21] prefer to design in-house dynamometer solutions for measuring UAV propeller performance which has shown to provide greater versatility in terms of specific design applications and accuracy. In 2019, a decision was made to design a custom-built thrust stand catered to Coanda UAV research. That was the objective of the 2019–2020 Senior Mechanical Engineering Capstone group at the University of Arkansas at Little Rock. Their task was to design a vertically oriented thrust stand which not only measured propeller thrust but could arrest a full-scale prototype of a Coanda UAV, thus allowing the measurement of the overall thrust generated by the prototype.
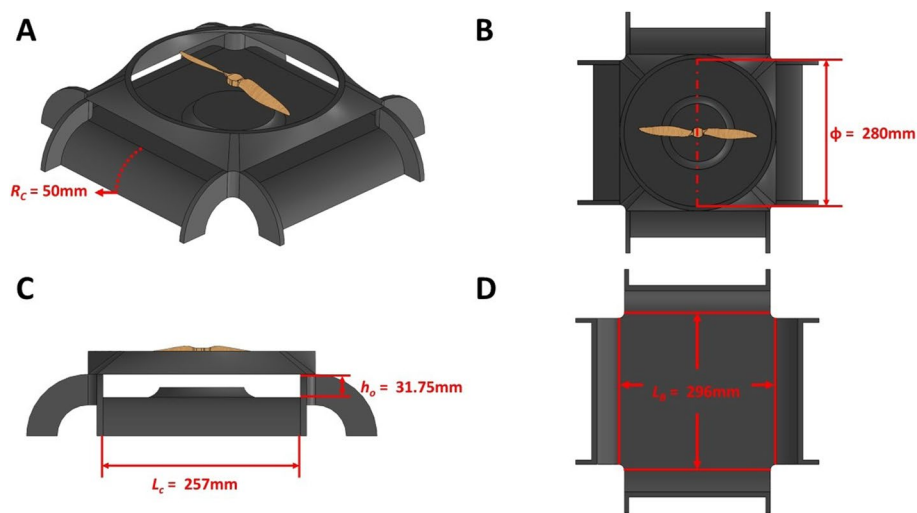
Once the thrust stand was successfully assembled and tested, the next stage involved using commercially available CFD simulation software to validate the experimental results. ANSYS Fluent™, a product of Dassault Systems, offers robust and cost-effective CFD simulation capabilities. To reduce computational costs, rotating propeller flow was simulated in steady state by employing the multiple reference frame (MRF) approach. The MRF approach involves segregating the fluid domain in two portions: (1) a stationary air domain and (2) a disk-shaped rotating domain. The rotating domain simulates the flow around a propeller by assigning a constant rotational speed to the surrounding fluid. The solid structure of the propeller itself remains fixed, and hence, this approach is also referred to as the "frozen rotor approach." This approach [22–24] has exhibited reliable accuracy in simulating propeller flow for small-scale multi-rotor UAVs.

## Methods

### Novel Coanda UAV: design, assembly, and construction

The novel design incorporates a four-sided linear arrangement of the Coanda surfaces having guide vanes on each end and centered around a $9 \times 6$ propeller. Such a design minimizes the area change in the radial direction as the fluid flows from the orifice towards the trailing edge of the Coanda surface. The length of each Coanda surface ($L_C$) and sides of the UAV baseplate ($L_B$) are shown in Fig. 1C and D, respectively.

In a preliminary two-dimensional CFD study [25], the optimum ratio of the orifice height ($h_o$) to the Coanda radius of curvature ($R_c$) was found to be within the range 0.25 $< h_o/R_c <$ 0.35. A prototype of the drone was designed with a $h_o/R_c$ ratio of 0.25. However, this design caused significant buildup of high pressure near the orifice which led to reduced Coanda thrust. This is because the incoming two-dimensional airflow in the
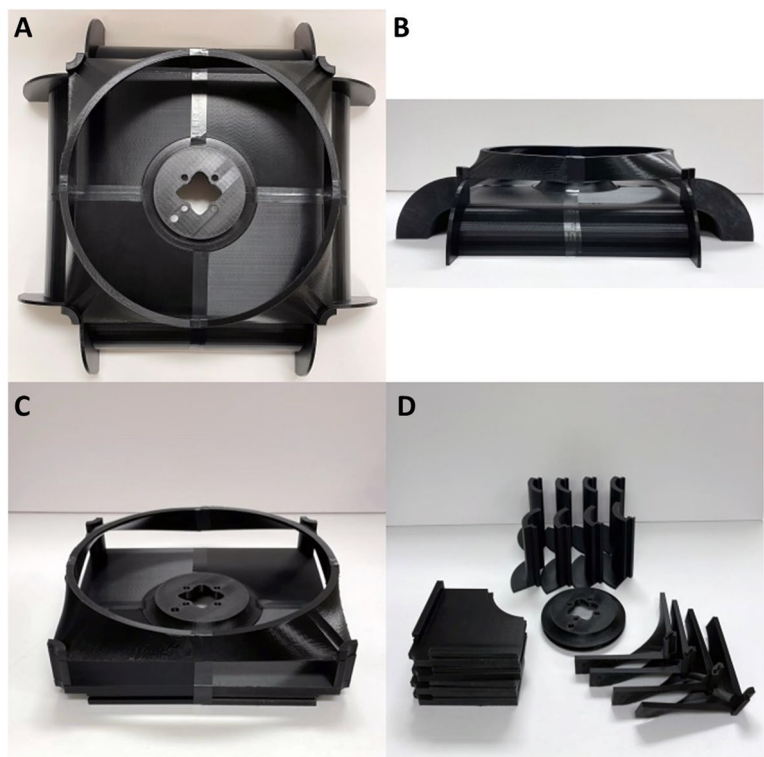
**Fig. 1** **A** Orthographic view, **B** top vie, **C** side view, and **D** bottom view of our device
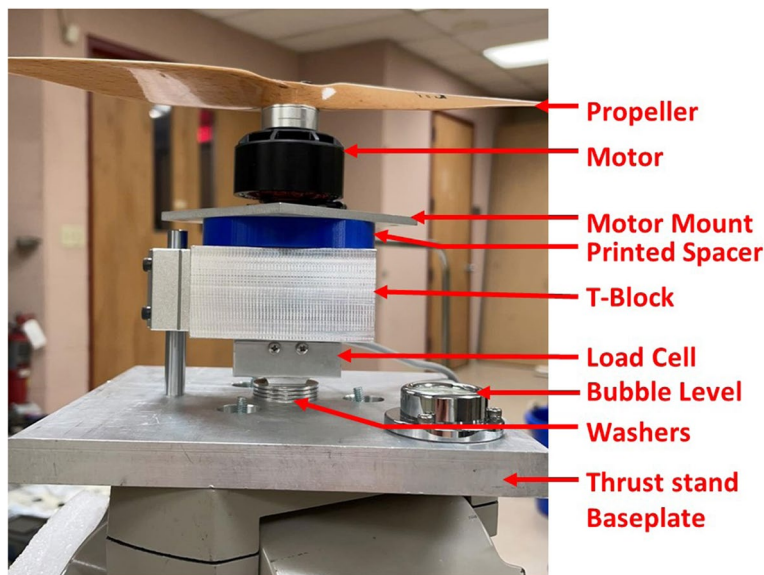
preliminary study [25] was parallel to the UAVs baseplate; thus, it did not represent propeller downwash conditions where the incoming vortex was perpendicular to the UAVs baseplate. To relieve the pressure near the orifice, the value of $h_o$ was increased from 12.5 to 31.75 mm. With a $h_o/R_c$ ratio of 0.63, a CAD model of the prototype was drafted in SolidWorks™ with $h_o = 31.75$ mm and $R_c = 50$ mm as shown in Fig. 1A and C. The fabrication of the prototype began with 3D printing symmetrical segments of the drone which were small enough to be printed on the FlashForge Inventor® series of printers as shown in Fig. 2. Grounded testing did not require the prototype to be made of ultra-lightweight materials. Hence, for durability reasons, the segments were printed using PLA plastic having 5% infill. The segments were mechanically fastened using guides, insets, and connectors. Small gaps between the assembled segments were covered with electrical tape to prevent airflow leakages. CAD model of the propeller was drafted using the Clark-Y airfoil shape.

**Experimental setup: Coanda thrust stand**

The components of the Coanda thrust stand, as shown in Fig. 3, were mounted on a survey tripod as it provides a stable and leveled platform. A low-profile tension-link load cell was fastened to the thrust stand baseplate with a maximum rated output of 25 lbs (11 kg). To cancel the effects of propeller torque, a square aluminum T-block transferred the twisting forces away from the load cell through a shaft extruding from the baseplate. The load cell measured forces acting solely on the T-block. A threaded screw ensured that a mechanical link was established between the load cell and T-block via a cavity drilled halfway through its center. Four threaded screws linked the top portion of the T-block with the motor mount, and a 10-mm 3D-printed spacer in the middle provided clearance from the extruded shaft. A Xoar™ 9 × 6 was coupled with a 505 kV brushless electric motor. The motor was connected to an 80-A Electronic Speed Controller (ESC) device where the latter drew stable and continuous electricity from a 30 V/10 A variable DC power supply. LabVIEW™ provided the necessary signal translation and graphical
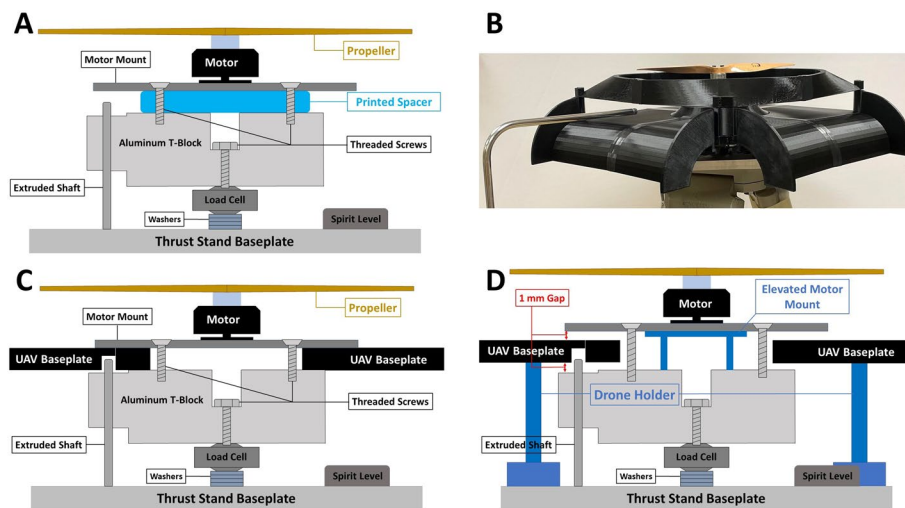
**Fig. 2**  **A** Top view of assembled prototype, **B** side view, **C** assembled prototype without Coanda surfaces, and **D** disassembled segments



**Fig. 3**  Coanda thrust stand components

user interface (GUI) capabilities. The analog signals from the load cell and RPM sensor (connected to 2 ESC poles) were routed through a NI-USB 6351 data acquisition (DAQ) device. Motor speed control was achieved by sending a pulse-width modulated

**Fig. 4 A** Cross-sectional schematic diagram of loading condition 1, **B** experimental setup for the loading condition 3, **C** cross-sectional schematic diagram of loading condition 3, **D** cross-sectional schematic diagram of loading condition 4

(PWM) signal from LabVIEW™ to the ESC via an Arduino. The load cell generated signals within a 2-mV range, while the NI DAQ device could only read signals above 0.1 V. A signal conditioner utilizing the INA-125 integrated circuit boosted the load cell signals to a DAQ-readable range while simultaneously reducing noise amplification. The load cell calibration procedure involved developing a linear relationship between the load cell output signal against a set of scaled weights applied in tension. The resulting $y = mx + b$ equation was programmed in LabVIEW™ to translate the load cell output signal in terms of force measured in Newton (N). In addition to thrust and RPM, another important parameter taken into consideration for CFD validation was downwash airspeed. This parameter was measured by using a pitot-tube connected to a PCE-HVAC 2 multifunction manometer module. The DAQ device and manometer module streamed the required data to a desktop PC, and to ensure operator safety, a transparent protective barrier was placed between the thrust stand and the PC [26].

After the load cell was calibrated, the experimental trials were conducted under four different loading conditions. Five trials were performed for each condition. Each trial consisted of measuring the averaged value of propeller thrust and downwash airspeed by maintaining a constant RPM for 15 s. In each trial, the RPM was fixed at three intervals near 4000 RPM, 6000 RPM, and 8000 RPM. The details of the four loading conditions are provided below.

### *Loading condition 1: propeller thrust*
This condition measured the standalone thrust generated by the 9 × 6 inch propeller as shown in Fig. 4A. The pitot tube was located at a propeller radial distance of 0.78 r/R and at a downstream location of 0.68 z/R. Here, *R* represents propeller radius (0.114 m), *r* represents the horizontal distance from the propeller hub (0.089 m), and *z* represents the vertical distance from the propeller hub (0.077 m).

### Loading condition 2: without Coanda surface thrust

The second loading condition called for measuring the combined thrust generated by the propeller and the UAV's baseplate. This was accomplished by mounting the assembled prototype without the Coanda surfaces between the T-block and motor mount as shown in Fig. 2C. The pitot tube measured the airspeed from one rectangular orifice and was located at its center as shown in Fig. 4B. This location was maintained for loading conditions 3 and 4.

### Loading condition 3: overall net thrust

The third condition, as shown in Fig. 4B, involved mounting the assembled prototype along with the Coanda surfaces between the motor mount and T-block. This condition measured the overall net thrust generated by the prototype. The contribution of the linear Coanda surfaces to the lift generation process was highlighted upon comparing experimental thrust results from loading conditions 2 and 3. To distinguish loading conditions 3 and 4, a cross-sectional schematic diagram for both is shown in Fig. 4C and D.

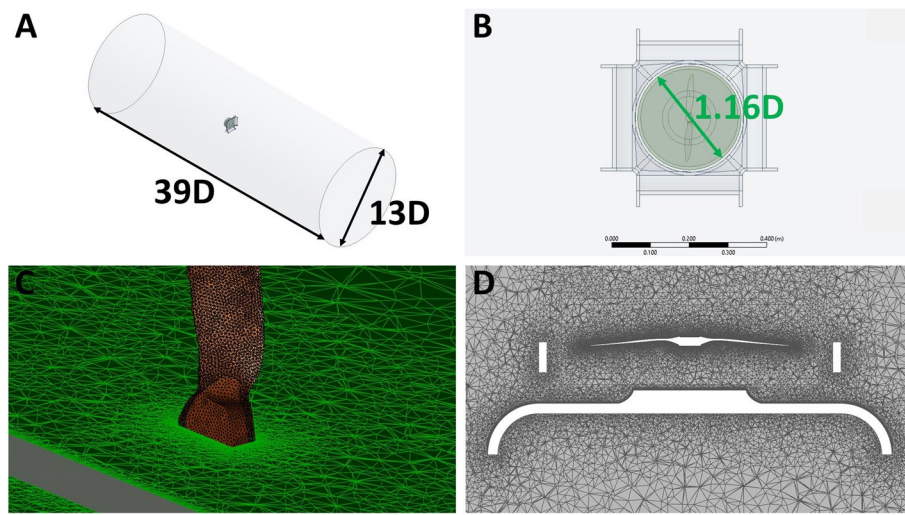### Condition 4: isolated propeller thrust

The last loading condition involved measuring propeller thrust while transferring the forces generated by the prototype's structure away from the T-block. Since the objective was to mechanically isolate and measure propeller thrust in the presence of the prototype's structure, this loading condition is referred to as "isolated propeller." To accomplish this, the prototype sat on a drone holding structure that transferred its weight to the thrust stand's baseplate while maintaining a 1-mm gap between the prototype and T-block. An elevated motor mount was then placed on the T-block and ensured a 1-mm gap between the prototype and the motor mount. The schematic diagram in Fig. 4D provides a cross-sectional view of the final loading condition.
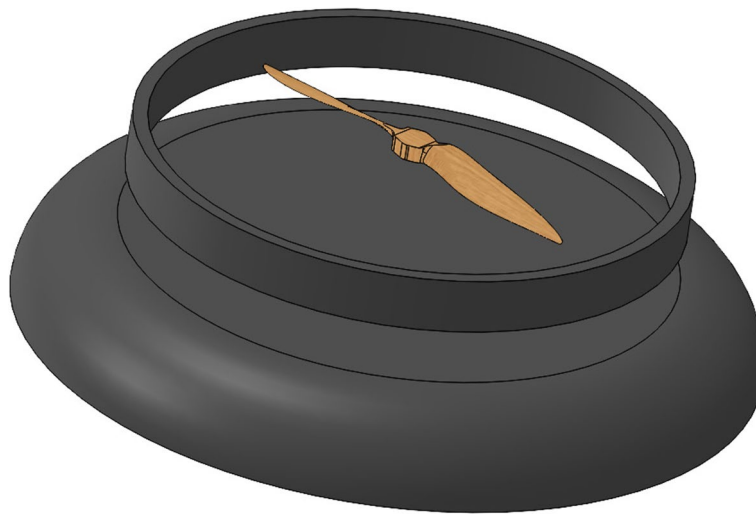
### System accuracy and errors

This section briefly describes the uncertainties associated with the instruments and sensors used in the experimental setup. The accuracy of the load cell (LC) is defined in terms of its nonlinearity error, repeatability error, and hysteresis. This involved performing a 5-point calibration procedure based on the load cell's maximum rated output (RO). The LC was subjected to tensile load at 0%, 50%, 100%, 50%, and 0% RO. The LC had a nonlinearity error of $\pm$ 0.15% RO, repeatability error of $\pm$ 0.05%, and hysteresis of $\pm$ 0.15% RO. The accuracy of the RPM sensor was determined by comparing the results with a laser tachometer at varying rotational speeds and was found to be around $\pm$ 1 RPM. The multifunction manometer module came calibrated from the manufacturer and had an accuracy of 0.3% reading at 25 °C, hysteresis of 0.3%, and resolution of 0.01 m/s.

### CFD setup

The CFD validation process involved performing steady-state MRF simulations on two different fluid domains at 4000 RPM, 6000 RPM, and 8000 RPM. The dimensions

**Fig. 5** **A** Dimensions of stationary domain, **B** diameter of frozen region, **C** meshes near propeller surface, and **D** cross-sectional mesh plane for second fluid domain



**Fig. 6** CAD model of conventional UAV

of the rotating and stationary domains were based on established literature and experience gained from the precursor study [23, 24]. As shown in Fig. 5A, the stationary domain is cylindrical in shape having a diameter of 13 D with a height of 39 D, where D is the propeller diameter. Similarly, the diameter of the rotating domain is 1.1 D, as shown in Fig. 5B, with a thickness of 0.4 D. In both fluid domains, the propeller was modeled within the rotating domain, while in the second domain, only the prototype was modeled within the stationary domain. The first fluid domain served to validate experimental results from loading condition 1. Similarly, the second fluid domain served to validate experimental results from loading conditions 2, 3, and 4 since Fluent® provided the versatility to measure forces across selected surfaces.

After the validation process, the next step was to evaluate the performance of the novel design with a conventional UAV as shown in Fig. 6. To prevent airspeed reduction due to viscous losses, the baseplate diameter of the conventional design was kept the same as the length of the novel design's baseplate ($L_B$). A conventional UAV, having the same $h_o/R_c$ ratio as the novel design, was modeled within the stationary domain to provide a numerical comparison between the novel and conventional designs across an expanded rotational speed regime (2000–12,000 RPM). The performance was evaluated in terms of thrust generated per the side surface area or the active Coanda surface area for both designs. The active Coanda surface area for novel and conventional design is 807.38 cm$^2$ and 887.43 cm$^2$, respectively. This comparison would serve as the basis for evaluating the recovery of fluid momentum losses in the radial direction experienced in conventional designs.

### Mesh generation and turbulence modeling

A systematic mesh refinement process was applied for conducting a grid independence study by monitoring the change in propeller thrust after every converged simulation. The criteria for achieving a grid independent solution was when the percentage difference in propeller thrust between two converged simulations of increasing mesh densities was less than 5%. Using unstructured tetrahedral elements, the process started with increasing the number of elements near the propeller surface from 50,000 elements to 5 million elements using a face sizing function. A mesh independent solution was achieved for the propeller surface at approximately 1 million elements with an element size of 0.0009 m. While maintaining this mesh density near the propeller surface, the same process was applied towards the surrounding fluid within the rotating domain. An intrinsic limitation of the MRF approach is the abrupt pressure-velocity change observed when the fluid transitions from stationary to rotating domain via the domain interfaces [27]. Therefore, it was imperative to ensure smooth transition and consistent mesh density near the interface region. The rotating domain was encased within another frozen cylindrical domain, and the objective was to increase the mesh density within this frozen region by applying a body of influence (BOI) grid-sizing function. This ensured a consistent mesh density within and outside the domain interfaces. The number of elements within this frozen region was again increased from 50,000 elements to 5 million elements. A mesh independent solution was achieved for the frozen region and rotating domain at approximately 1.5 million elements with an element size of 0.0075 m. The final step involved increasing the mesh density in the stationary domain using a body sizing function. While increasing the mesh density within the stationary domain from 50,000 elements to 5 million elements, no change in propeller thrust was observed. However, 500,000 elements were nonetheless added to the stationary domain to generate a mesh with acceptable overall values of element quality and element skewness. Therefore, the resulting mesh size that provided a grid independent solution for the first domain is approximately 3 million elements. For the second fluid domain, an additional step was performed for a grid independent solution near the prototype's walls while measuring thrust from one of the Coanda surfaces. The mesh density near the prototype's walls was increased from 50,000 elements to 5 million elements using a face sizing function. A mesh independent solution was achieved at approximately 3 million elements with an

element size of 0.003 m. Thus, the resulting mesh size that provided a grid independent solution for the second fluid domain is approximately 6 million elements.

Steady-state CFD simulations involved numerically solving Reynold's-averaged Navier-Stokes (RANS) equation through turbulence models. In this study, the two-equation K-Epsilon ($k$-$\epsilon$) realizable turbulence model was selected which exhibited reliable performance in predicting turbulent flows while applying the MRF approach [27–31]. First proposed by Shih et al. [32] as a modification to the standard $k$-$\epsilon$ model, the $k$-$\epsilon$ realizable model is well suited for simulating turbulent flows in rotation as well as capturing boundary layer separation and recirculation effects. Sagol et al. [33]'s assessment of the two turbulence models showed that the $k$-$\epsilon$ realizable model provided better agreement with experimental wind turbine data when compared to the standard $k$-$\epsilon$ model. Near-wall turbulence modeling becomes a challenge as it requires high-resolution meshes to capture the viscous sub-layer region [34]. To reduce computational complexity, wall functions were employed to dictate fluid behavior at the viscous sub-layer level. Through inflation layers, the mesh resolution was resolved up to the buffer layer where the values of $y^+$ lie between 5 and 30 [35]. Scalable wall functions provided the flexibility to displace mesh $y^+$ values to 11.225 since smaller values of $y^+$ were found near the propeller walls, while the opposite was true near the walls of the prototype [36]. Before proceeding to the simulations, the residual convergence criteria were lowered from $1e^{-3}$ to $1e^{-4}$ and $1e^{-5}$. When no significant change was observed in the final thrust values, the convergence criteria were reverted to $1e^{-3}$ to reduce computational costs. The SIMPLE solver was used for pressure velocity coupling. The SIMPLE solver has demonstrated reliable performance for a variety of MRF applications such as UAV propellers [22, 23], marine propellers [37], wind turbines [38], centrifugal pumps [39], and tidal turbines [40]. The numerical setup for CFD simulations is provided in Table 1.
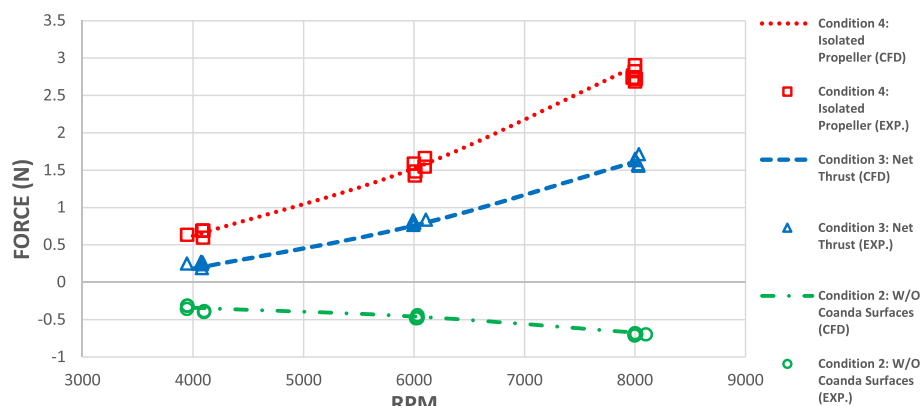
## Results

### Validation and analysis

Thrust results from 4000 to 8000 RPM for loading conditions 2, 3, and 4 are shown in Fig. 7. Loading condition 1 (propeller) and loading condition 4 (isolated propeller) showed similar thrust values; hence, in Fig. 7, they were omitted for clarity. The airspeed results for loading conditions 2, 3, and 4 displayed a similar pattern; hence, Fig. 8 shows the plots for loading conditions 1 and 2. CFD results provided good overall agreement with the experimental results based on the visual inference of Figs. 7 and 8. To quantify how accurate CFD simulations predicted experimental conditions, the mean absolute percentage errors (MAPE) for all four loading conditions are tabulated in Table 2. MAPE results showed that between CFD and experimental results, errors for both parameters were less than 8%. Based on Paz et al. [41]'s CFD simulation of a quadcopter UAV (having similar propeller size and using the same turbulence model), the thrust difference between the MRF and experimental data was close to 11%. Thus, the MRF results in this study were deemed to be well within the range of acceptable accuracy.
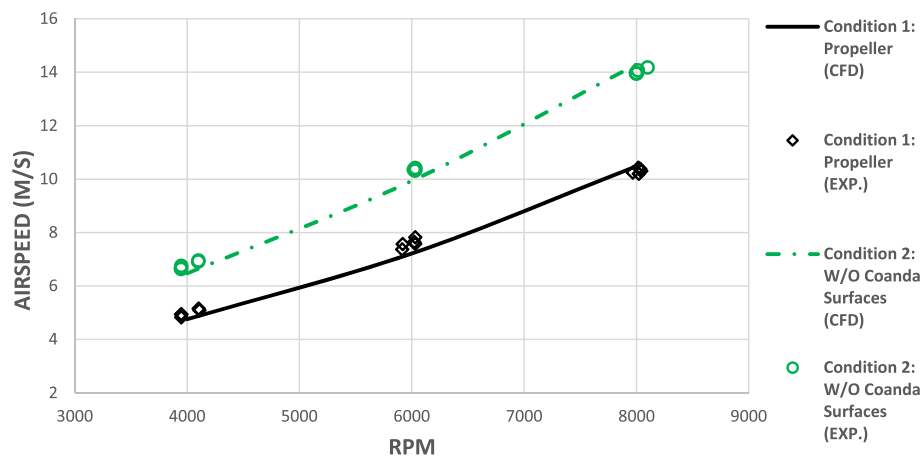
An intrinsic limitation of Coanda-based UAVs is the reduction in lift when compared to a standalone propeller. For example, at 8000 RPM, Naudin's UAV generated 6.2 N of thrust, whereas the standalone propeller generated 9.4 N of thrust. This amounted to a 34 % reduction in overall net thrust. From CFD simulations, the force

**Table 1** Numerical setup of CFD simulations

| | |
|---|---|
| Solver settings | |
|   Type | Pressure based |
|   Velocity formulation | Absolute |
|   Time | Steady |
| Models | |
|   Energy equation | Disabled |
|   Turbulence model | $k\text{-}\epsilon$ realizable |
|   Near-wall treatment | Scalable wall functions |
| Materials | |
|   Fluid | Air |
|   Density | 1.225 kg/m$^3$ |
|   Viscosity | 0.000017894 kg/m.s |
| Cell zone conditions | |
|   Rotating domain | Frame motion |
|   Rotating axis direction | X-axis |
| Boundary conditions | |
|   Inlet | Pressure inlet |
|   Outlet | Pressure outlet |
|   Propeller | Moving wall (rotation along x-axis) |
|   Domain walls | Walls |
| Solution settings | |
|   Pressure-velocity coupling scheme | SIMPLE |
|   Gradient | Least-squares cell based |
|   Pressure | Second order |
|   Momentum | Second order |
|   Turbulent kinetic energy | Second-order upwind |
|   Turbulent dissipation rate | Second-order upwind |
|   Initialization | Standard initialization |



**Fig. 7** Thrust vs RPM results for loading conditions 2, 3, and 4

distribution across various surfaces of the novel design from 4000 to 8000 RPM is tabulated in Table 3. When compared to standalone propeller thrust of 3.05 N at 8000 RPM (from loading condition 1), the percentage thrust reduction experienced by the novel design was close to 46% (1.61 N). At 8000 RPM, the baseplate's contribution

**Fig. 8** Airspeed vs RPM results for loading conditions 1 and 2

**Table 2** Thrust and airspeed MAPE results for all four loading conditions

|  | Mean absolute percentage error (%) | | | |
|---|---|---|---|---|
|  | **Propeller** | **Without Coanda surface** | **Overall** | **Isolated propeller** |
| Thrust | 4.3% | 6.7% | 5.4% | 7.8% |
| Airspeed | 3.3% | 7.9% | 6.1% | 4.1% |

**Table 3** CFD force distribution across different surfaces of novel design from 4000 RPM to 8000 RPM

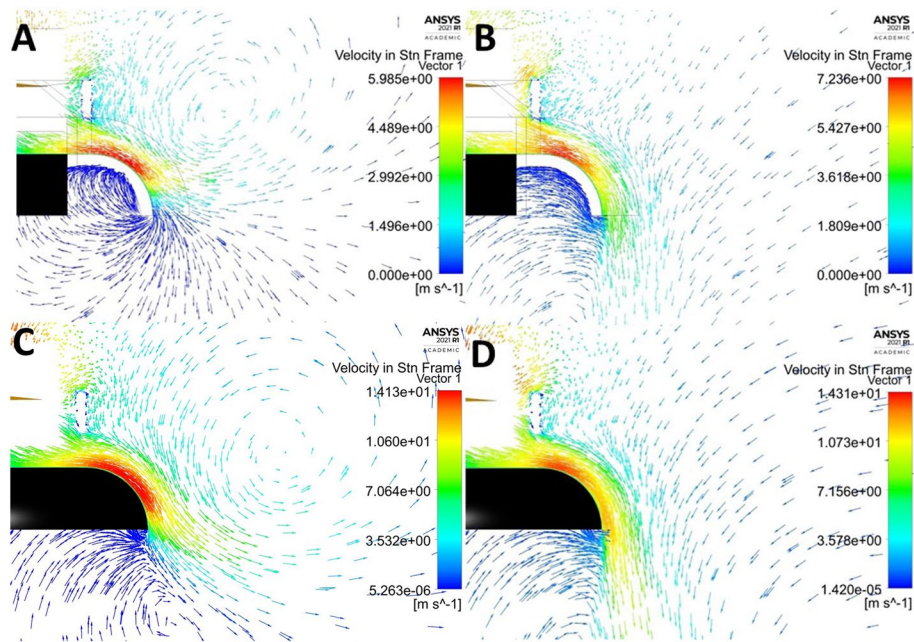| Rotation speed (RPM) | Propeller (*N*) | Baseplate (*N*) | Coanda surfaces (*N*) | Overall thrust (*N*) |
|---|---|---|---|---|
| 4000 | 0.62 | 0.96 | 0.52 | 0.18 |
| 6000 | 1.52 | 1.98 | 1.21 | 0.75 |
| 8000 | 2.88 | 3.55 | 2.28 | 1.61 |

was around 41% (3.55 N), while the propeller and Coanda surface's contribution was 33% (2.88 N) and 26% (2.28 N), respectively. Figure 7 also shows that the baseplate generated higher values of negative thrust due to increase in downwash airspeed as the RPM increased. From Fig. 8, it is observed that the values of airspeed for loading condition 1 (standalone propeller) were higher than that of loading condition 2 (without Coanda surface). This observation is attributed to the viscous losses incurred by the fluid as it flows over the baseplate.

### Numerical comparison

Figure 9 presents the numerical comparison between novel and conventional designs from 2000 to 12,000 RPM in terms of thrust per side surface area. Results show that the conventional design did not generate lifting forces greater than 5 N/m$^2$ from 2000 to 4000 RPM, while the novel design produced a lift force of 6.4 N/m$^2$ at 4000 RPM. At 6000 RPM, both designs produce lift forces greater than 10 N/m$^2$. When the percentage

**Fig. 9** Thrust per side surface area vs RPM for novel and conventional design



**Fig. 10  A** Novel design velocity vectors at 2100 RPM, **B** novel design velocity vectors at 4000 RP, **C** conventional design velocity vectors at 6000 RPM, and **D** conventional design velocity vectors at 8000 RPM

increase in lift forces or thrust per side surface area from 6000 to 12,000 RPM was averaged, the novel design exhibited a 17% improvement over the conventional design.
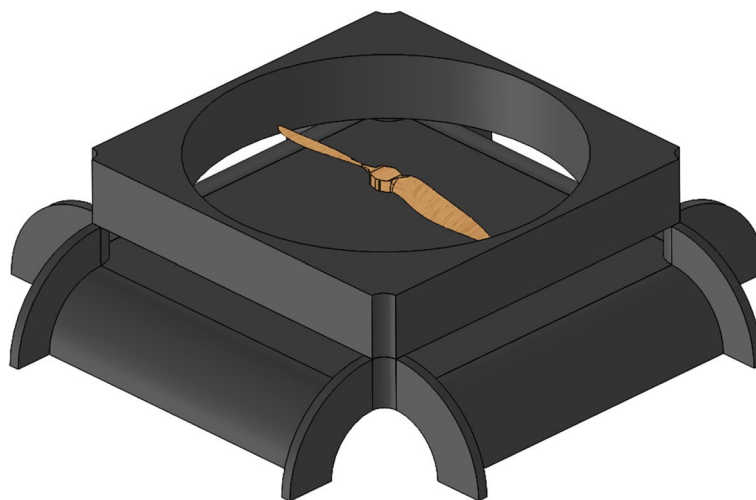
One possible explanation for the novel design's efficiency can be observed through visual inference of velocity vector plots. In conventional saucer-shaped UAVs, flow separations along the Coanda surface are a common occurrence [42]. Many designers have used vortex generators and axial vanes to prevent or delay flow separations such that the flow remains attached to the curved surface [43]. Najafi et al. [44] investigated the application of axial vanes on Naudin's UAV [7] along its separation points. Through experimental

trials and 2D CFD simulations, Najafi et al. [44] observed that without axial vanes, the flow separations occurred at a propeller rotational speed of 7320 RPM. To investigate flow separations for this study, velocity vectors were plotted across the midplane as shown in Fig. 10. Velocity vector plots show that the conventional UAV experienced separations occurred at 6000 RPM (Fig. 10C) which is closely consistent with Najafi et al. [44]'s observation after which stable Coanda flow was achieved at 8000 RPM (Fig. 10D). A stable Coanda flow is when the blanket of high velocity air remains attached to the contours of the convex Coanda surfaces without experiencing flow separations. Meanwhile, flow separations in the novel design occurred at 2100 RPM (Fig. 10A), and a stable Coanda flow was achieved at 4000 RPM (Fig. 10B). The flow separations shown in Fig. 10A and C are characterized by a swirling vortex generated above the Coanda surface. This early recovery of Coanda flow could be attributed to the recovery of fluid momentum losses in the radial direction; however, this phenomenon needs to be studied more extensively, the details of which are mentioned in the "Discussion and future work" section.

## Discussion and future work

Now as the novel design has demonstrated an effective recovery of thrust losses in the radial direction, the next step will encompass designing a flying prototype. However, certain limitations in the existing design are needed to be addressed before arriving at this stage. The primary concern was to address the reduction in overall net thrust due to the baseplate. As mentioned previously, Naudin's UAV [7] exhibited a 34% reduction in overall net thrust compared to a standalone propeller. The goal was to bring the percentage reduction in overall thrust for the novel design down to a level that matches Naudin's UAV [7]. Using the CFD design tool developed in this study, it was observed that for the novel design, a flat baseplate generated the least negative thrust when compared to a concave and convex baseplate. The canopy was also redesigned to induce more pressure within the chamber. The new design, shown in Fig. 11, has a flat baseplate with a redesigned canopy. At 8000 RPM, the redesigned UAV generated 1.9 N of thrust which constituted a 36% reduction in overall net thrust. Naudin's original design [7] used a



**Fig. 11** Redesigned UAV with flat baseplate and modified canopy

10-inch propeller having a pitch of 7 inches. The future novel flying prototype will also be scaled up to accommodate a propeller of similar dimensions and incorporate the design revisions detailed in Fig. 11. Another considered design factor will be the application of coaxial contrarotating propellers instead of a single-rotor propeller. There are several benefits associated with using contrarotating propellers when compared to single propellers such as increase in overall thrust, effective cancellation of propeller torque, and higher downwash airspeeds [45]. In theory, the higher downwash airspeeds from contrarotating propellers would give rise to higher thrust from the Coanda surfaces. The actual flying prototype will also take advantage of lightweight 3D printable construction materials such as carbon fiber to reduce the overall weight of the UAV structure.

For evaluating the performance of a Coanda-based UAV, this study demonstrates the efficacy of applying the MRF approach coupled with the $k$-$\epsilon$ realizable turbulence model. Such a technique has been shown to provide accurate results for a quadcopter UAV [41]. In terms of thrust, the highest errors were associated with loading condition 4 (7.8%) and the lowest with loading condition 1 (3.4%). In terms of airspeed, the highest errors were associated with loading condition 2 (7.9%) and the lowest with loading condition 1 (3.3%). In addition to validating experimental results of this study, CFD results of the conventional design correlated with Barlow et al. [14] and Najafi et al. [44]'s experimental results for Naudin's UAV [7]. At 8000 RPM, CFD simulations revealed that the percentage decrease in overall thrust (2.32 N) compared to the standalone propeller (3.05 N) for the conventional design was close to 24%. It should be noted that the conventional design in this study is an idealized Coanda design which does not contain structures that obstruct airflow towards the orifice such as supports and vanes. The viscous losses (Fig. 8) and idealized design could explain the discrepancy in percentage thrust reduction of the conventional design (24%) and Naudin's UAV [7] (34%). The conventional design also displayed flow separations occurring at 6000 RPM, which is close to Najafi et al. [44]'s observations at 7320 RPM for Naudin's UAV [7] without axial vanes, albeit with a different Coanda radius, orifice height, and propeller size.

There are certain limitations associated with the current hardware used for the experimental setup. The 30 V/10 A variable DC power supply is unable to push the motor beyond 8000 RPM. At 9.9, the motor maxes out at 8200 RPM. To design a prototype that will be scaled up to accommodate a 10-inch propeller, a 30 V/30 A power supply would be sufficient to push the motor towards attaining higher rotational speeds. Current CFD simulations showed flow separations occurring at much lower rotational speeds in the novel design. To study and verify this phenomenon in more detail, future hardware investments would include integrating a fog dispensing system into the experimental setup. This would provide the capability to visualize flow separations experimentally for different Coanda surfaces, having different radii, and validate them with CFD simulations. The addition of a flow visualization system to the current setup would also assist in studying airflow near the wake region of the UAV. The thrust stand will also be modified to include provisions for a coaxial rotor. This will include modifying the T-block and motor mount such that both structures are more streamlined. The system will also incorporate pressure transducers located at different radial distances of the Coanda surfaces to capture the pressure/force distribution. These pressure transducers would be able to provide a more detailed analysis regarding the recovery of fluid momentum and thrust generation along the radial direction.

The novel design opens new potential for adding various Coanda UAV-related upgrades. One such upgrade involves directly addressing the negative thrust produced by the baseplate. Barlow et al. [14] investigated the use of a unique propulsion system based on the Dyson Air Multiplier™ concept which is known as the ring-wing airfoil propulsion system. Such a propulsion system would use an enclosed air compressor to ensure that the incoming air is parallel to the baseplate instead of being perpendicular as is the case with using a propeller. Barlow et al. [14]'s application of a ring-wing airfoil on a radial UAV yielded less than favorable results. However, it is likely that due to thrust losses in the radial direction experienced in conventional Coanda UAVs, applying the ring-wing airfoil would offer more favorable results for the novel design. The design parameters, with regard to the optimal $h_o/R_c$, for a future prototype using a ring-wing airfoil system are reflected in the preliminary 2D CFD study [25] mentioned previously. This is because the actual flow conditions would resemble more closely to the preliminary study [25]. Work is underway at the University of Arkansas at Little Rock to design an air compressor-type ring-wing airfoil propulsion system for the novel Coanda UAV with a $h_o/R_c$ ratio of 0.25. Recently, the stealth capabilities offered by Coanda UAVs are also gaining traction. Shun et al. [46] observed that the addition of weight-saving techniques coupled with 3D-printed anti-noise materials on Naudin's UAV [7] reduced the acoustic signature of the UAV by 16 times. Using propellers with higher rotor twist and taper also improves the acoustic performance of a UAV [47]. Such similar characteristics could also be observed in the novel design. In addition to reduced acoustic signature, the novel design could (in theory) yield a more reduced radar cross section (RCS) signature since it has more angular and rectangular surfaces.

## Conclusion

A novel Coanda UAV is proposed in this study specifically designed to alleviate the thrust losses experienced in conventional Coanda UAVs in the radial direction. The novel design employed a rectangular, linear arrangement of the Coanda surfaces to minimize the area change in the radial direction. For grounded testing, a prototype UAV was 3D printed using symmetrical segments and assembled around a single $9 \times 6$ propeller. A custom-built thrust stand and a pitot were used to measure thrust and downwash airspeed under four different loading conditions: (1) standalone propeller, (2) without Coanda surfaces, (3) overall prototype thrust, and (4) isolated propeller thrust. Thrust and airspeed data were recorded for 40 trials conducted from 4000 to 8000 RPM. The experimental trials were validated using CFD simulations while applying the MRF approach in steady state. Using the $k$-$\epsilon$ realizable turbulence model, the experimental results were validated with MAPE values less than 8% for both thrust and airspeed. A numerical comparison between the novel design and conventional design of similar dimensions was carried out using CFD simulations conducted from 2000 to 12,000 RPM. Results showed that the novel Coanda design offered 17% improvement in thrust per the side Coanda surface area, demonstrating an effective reduction of the thrust losses in the radial direction beyond 6000 RPM. Revisions to the novel design are proposed which will attempt to yield similar performance characteristics to existing Coanda UAV designs. The redesigned UAV will be used as the foundation for building a flying prototype in the near future.

## Nomenclature

$L_C$ — Length of Coanda surface
$L_B$ — Side length of the UAV baseplate
$h_o$ — Orifice height
$R_c$ — Coanda radius of curvature
$y^+$ — Wall y plus

**Abbreviations**
CFD — Computational fluid dynamics
MRF — Multiple reference frame
DC — Direct current
ESC — Electronic speed control
PWM — Pulse-width modulated signal
UAV — Unmanned aerial vehicle
DAQ — Data acquisition device
RPM — Rotations per minute
PLA — Polylactic acid plastic
GFS — Geoff's flying saucers
RO — Rated output
MAPE — Mean average percentage error
$L_C$ — Length of Coanda surface
$L_B$ — Side length of the UAV baseplate
$h_o$ — Orifice height
$R_c$ — Coanda radius of curvature
$y^+$ — Wall y plus

## Declarations

**Ethics approval and consent to participate**
Not applicable.

**Competing interests**
The authors declare that they have no competing interests.

## References

1. Ayamga M, Akaba S, Nyaaba AA (2021) Multifaceted applicability of drones: a review. Technol Forecast Soc Change 167:120677. https://doi.org/10.1016/J.TECHFORE.2021.120677
2. Ionică C, Sorin D (2010) Review of applications on Coandă effect: history, theories, new trends. Rev Air Force Acad 2:14–21
3. Ahmed RI, Djojodihardjo H, Abu-Talib AR, Mohd-Rafie A (2017) Review on progress and application of active flow control devices-Coandă effect on unmanned aerial vehicles. Pertanika J Sch Res Rev 3(1):2462–2028
4. Collins RJ (2002) Coanda - a new airspace platform for UAVs. In: Seventeenth International Conference 2002. Bristol University UK. Unmanned Air Vehicle Systems, Bristol
5. Collins RJ (2003) Aerial devices
6. Hatton G (2009) Advanced air vehicle

7.  The GFS-UAV model N-01A, Full plan and construction details by Jean-Louis Naudin. http://jlnlabs.online.fr/gfsuav/gfsuavn01a.htm. Accessed 13 Sept 2021
8.  Nedelcut F (2010) Coanda effect UAV – a new born baby in the unmanned aerial Vehicles family. Rev Air Force Acad 17(2):21–28. https://doi.org/ISSN:1842-9238.17
9.  Lee JW (2018) A thrust generator for Vertical Take-Off and Landing (VTOL) aerial vehicles. 62/754,085, November 2018
10. Jay Drones L.L.C. | Agriculture | F6S Profile. https://www.f6s.com/jaydronesl.l.c. Accessed 27 May 2022
11. Ahmed RI, Abu Talib AR, Rafie ASM, Djojodihardjo H (2017) Aerodynamics and flight mechanics of MAV based on Coandă effect. Aerosp Sci Technol 62:136–147. https://doi.org/10.1016/j.ast.2016.11.023
12. Hibbeler RC (2015) Fluid mechanics. Pearson Prentice Hall, Hoboken
13. Dinca L, Corcau JI, Larco CM et al (2019) About aerodynamic design of a Coanda effect UAV. In: 2019 7th E-Health and Bioengineering Conference, EHB 2019. Institute of Electrical and Electronics Engineers Inc., New York City, pp 1–4. https://doi.org/10.1109/EHB47216.2019.8969896
14. Barlow C, Lewis D, Prior SD et al (2009) Investigating the use of the Coanda effect to create novel unmanned aerial vehicles. In: International Conference on Manufacturing and Engineering Systems Proceedings. Middlesex University Research Repository, London, pp 386–391
15. Tyto Robotics, formerly RCbenchmark: motor & propeller thrust stands — Tyto Robotics Inc. https://www.tytorobotics.com/. Accessed 14 Sept 2021
16. Siddiqi Z, Lee JW (2022) A computational and experimental study on aerodynamics of motor-driven propellers using thrust stand and rotating cup anemometer. Prog Comput Fluid Dyn An Int J 22:23–36. https://doi.org/10.1504/PCFD.2022.120276
17. Hossain MR, Krouglicof N (2010) Propeller dynamometer for small unmanned aerial vehicle. In: Can Conf Electr Comput Eng. https://doi.org/10.1109/CCECE.2010.5575152
18. Gong A, Macneill R, Verstraete D (2018) Performance testing and modeling of a brushless dc motor, electronic speed controller and propeller for a small uav. In: 2018 Jt Propuls Conf https://doi.org/10.2514/6.2018-4584
19. Asson KM, Dunn PF (2012) Compact dynamometer system that can accurately determine propeller performance. 29:8–9 https://doi.org/10.2514/3.46118
20. Ravi A, Arena A (2011) UAV power plant performance evaluation. https://doi.org/10.2514/6.2011-1263
21. Conner JP, Arena AS (2002) Advanced dynamometer designed to fully characterize the propulsion system for a UAV. SAE Tech Pap. https://doi.org/10.4271/2002-01-2921
22. Pérez GAM, López OD, Escobar JA (2017) Computational study of the wake of a quadcopter propeller in hover. In: 23rd AIAA Comput Fluid Dyn Conf 2017, pp 1–9. https://doi.org/10.2514/6.2017-3961
23. Kutty HA, Rajendran P (2017) 3D CFD simulation and experimental validation of small APC slow flyer propeller blade. Aerospace 4. https://doi.org/10.3390/aerospace4010010
24. Stajuda M, Karczewski M, Obidowski D, Jóźwik K (2016) Development of a CFD model for propeller simulation. Mech Mech Eng 20:579–593
25. Kelly NQ, Siddiqi Z, Lee JW (2020) Computational fluid dynamics analysis and optimization of the Coanda unmanned aerial vehicle platform. In: World Academy of Science, Engineering and Technology, International Journal of Mechanical and Mechatronics Engineering, pp 532–537
26. Daniels D, Grimmett C, Kelly N, Mullen N (2020) 2019–2020 Capstone Design Project: Custom-Built Thrust Stand. University of Arkansas, Little Rock, pp 21–28
27. Li Y, Rowinski DH, Bansal K, Reddy KR (2018) CFD modeling and performance evaluation of a centrifugal fan using a cut-cell method with automatic mesh generation and adaptive mesh refinement. Int Compress Eng Conf 2622:1–8 https://doi.org/https://docs.lib.purdue.edu/icec/2622
28. Sabaeifard P, Razzaghi H, Forouzandeh A (2012) Determination of vertical axis wind turbines optimal configuration through CFD simulations. In: 2012 Int Conf Futur Environ Energy, vol 28, pp 109–113
29. Vijayanandh R, Ramesh M, Raj Kumar G et al (2019) Research of noise in the unmanned aerial vehicle's propeller using CFD. Int J Eng Adv Technol. https://doi.org/10.35940/ijeat.F1031.0886S19
30. Gullberg P, Löfdahl L, Nilsson P (2011) Fan modeling in CFD using MRF model for under hood purposes. In: ASME-JSME-KSME 2011 Jt Fluids Eng Conf AJK 2011, vol 1, pp 931–942. https://doi.org/10.1115/AJK2011-23020
31. Rahman M, Ahmed M, Soloiu V et al (2017) Investigation of aerodynamic performance of helical shape vertical-axis wind turbine models with various number of blades using wind tunnel testing and computational fluid dynamics. In: ASME 2016 Int Mech Eng Congr Expo IMECE 2016, vol 7, pp 11–17. https://doi.org/10.1115/IMECE2016-68081
32. Shih TH, Liou WW, Shabbir A et al (1995) A new k-ε eddy viscosity model for high Reynolds number turbulent flows. Comput Fluids 24:227–238. https://doi.org/10.1016/0045-7930(94)00032-T
33. Sagol E, Reggio M, Ilinca A (2012) Assessment of two-equation turbulence models and validation of the performance characteristics of an experimental wind turbine by CFD. ISRN Mech Eng 2012:1–10. https://doi.org/10.5402/2012/428671
34. Petit O, Nilsson H (2013) Numerical investigations of unsteady flow in a centrifugal pump with a vaned diffuser. Int J Rotating Mach. https://doi.org/10.1155/2013/961580
35. Salim SM, Ariff M, Cheah SC (2010) Wall y+ approach for dealing with turbulent flows over a wall mounted cube. Prog Comput Fluid Dyn. https://doi.org/10.1504/PCFD.2010.035368
36. Ferguson JD, Walters DK, Leylek JH (1998) Performance of turbulence models and near-wall treatments in discrete jet film cooling simulations. In: Proceedings of the ASME Turbo Expo
37. Subhas S, Saji VF, Ramakrishna S, Das HN (2012) CFD analysis of a propeller flow and cavitation. Int J Comput Appl Technol 55:26–33. https://doi.org/10.5120/8841-3125
38. Johansen J, Sørensen NN (2004) Aerofoil characteristics from 3D CFD rotor computations. Wind Energy 7:283–294. https://doi.org/10.1002/we.127
39. Wang ZJ, Zheng JS, Li LL, Luo S (2013) Research on three-dimensional unsteady turbulent flow in multistage centrifugal pump and performance prediction based on CFD. Math Probl Eng 2013. https://doi.org/10.1155/2013/589161

40. el Sheshtawy H, el Moctar O (2021) Numerical investigation of a tidal stream turbine using two methods of the multiple reference frame and the actuator disk momentum. J Adv Mar Eng Technol 45:275–287. https://doi.org/10.5916/JAMET.2021.45.5.275

41. Paz C, Suárez E, Gil C, Vence J (2021) Assessment of the methodology for the CFD simulation of the flight of a quad-copter UAV. J Wind Eng Ind Aerodyn 218:104776. https://doi.org/10.1016/J.JWEIA.2021.104776

42. Crivoi O, Doroftei I (2016) Some experimental results on Coanda effect with application to a flying vehicle. IOP Conf Ser Mater Sci Eng 147. https://doi.org/10.1088/1757-899X/147/1/012082

43. Gad-el-Hak M, Bushnell DM (1991) Separation control: review. J Fluids Eng 113:5–30. https://doi.org/10.1115/1.2926497

44. Najafi M, Jahanmiri M  An innovative technique to increase lift of a Coanda UAV. IOSR J Mech Civ Eng e-ISSN 14:27–35. https://doi.org/10.9790/1684-1402012735

45. Shukla D, Komerath N (2019) Drone scale coaxial rotor aerodynamic interactions investigation. J Fluids Eng Trans ASME 141. https://doi.org/10.1115/1.4042162/472973

46. Shin D, Kim H, Gong J et al (2020) Stealth UAV through Coanda effect. In: 2020 Fourth IEEE Int Conf Robot Comput, vol 1, pp 202–209. https://doi.org/10.1109/IRC.2020.00040

47. Henricks Q, Wang Z, Zhuang M (2020) Small-scale rotor design variables and their effects on aerodynamic and aeroacoustic performance of a hovering rotor. J Fluids Eng 142. https://doi.org/10.1115/1.4046872/1082419

**Publisher's Note**